INSTITUTE OF PHYSICS PUBLISHING JOURNAL OF PHYSICS: CONDENSED MATTER

J. Phys.: Condens. Matter **17** (2005) 3619–3635 doi:10.1088/0953-8984/17/23/014

A charge transfer ionic–embedded atom method potential for the O–Al–Ni–Co–Fe system

Xiao Wang Zhou[1] **and Haydn N G Wadley**

Department of Materials Science and Engineering, 116 Engineer's Way, University of Virginia, Charlottesville, VA 22904-4745, USA

E-mail: xz8n@virginia.edu

Received 4 January 2005, in final form 4 January 2005
Published 27 May 2005
Online at stacks.iop.org/JPhysCM/17/3619

Abstract

Magnetic tunnel junctions (MTJs) require the growth of a thin (∼20 Å) dielectric metal oxide layer, such as Al_2O_3, on a ferromagnetic metal layer, such as Co, CoFe, or CoNiFe. The atomic assembly mechanisms that combine to form a uniformly thin metal oxide layer on these metal surfaces are not well understood. The application of molecular dynamics simulations to the growth of metal and metal oxide multilayers that involve more than one metal element has not been possible using the conventional interatomic potentials. A recently proposed modified charge transfer ionic–embedded atom method potential appears to correctly enable the charge transfer between oxygen and numerous metal elements to be modelled in a format amenable for molecular dynamics studies. Here we parametrize this charge transfer ionic–embedded atom method potential for the quinternary O–Al–Ni–Co–Fe system so that a direct molecular dynamics simulation of the growth of the tunnelling magnetoresistive multilayers can be realized.

1. Introduction

Magnetic tunnel junctions (MTJs) composed of a thin (∼20 Å) dielectric oxide (such as AlO_x) [1–3] tunnel barrier layer sandwiched between ferromagnetic metals (such as Co, CoFe, or NiCoFe) [1, 2] exhibit large changes in electrical resistance when an external magnetic field is applied [4]. This tunnelling magnetoresistance (TMR) effect is being developed for a novel magnetic random access memory (MRAM) [1, 5–9]. The TMR effect can also be used for magnetic field sensing [2, 10, 11] and spin injection [12] in semiconductor devices [13].

The atomic scale structure of the oxide layer together with defects at the interfaces between the oxide and metal layers can significantly impact the performance of the devices described above. It has also been difficult to grow the ultra-thin oxide layers without incorporating

[1] Author to whom any correspondence should be addressed.

small holes in the layer. Because of this, MTJs usually have an oxide layer thickness above a threshold of about 10 Å [14, 15]. Efforts to reduce the oxide layer thickness are aided by a fundamental understanding of the atomic assembly and defect incorporation mechanisms during the growth of these metal and metal oxide multilayers. Molecular dynamics (MD) simulation of vapour deposition provides a potential means to achieve this understanding and has been successfully used to help study the vapour deposition of metal multilayers [16–18]. Its application to MTJ growth has been impeded by the lack of suitable interatomic potentials for multi-metal oxide systems.

Unlike close packed metal multilayers, atomic interactions in metal and metal oxide heterostructures can be either predominantly ionic or metallic depending on the local atomic surroundings. Because of this, MD simulations of oxidation must be carried out using a charge transfer interatomic potential [19, 20]. The initially proposed charge transfer potential [19, 20] did not include the physics of valence and as a result could only be used for single-metal–oxygen binary systems [21, 22]. By incorporating a simplified physics of valence, the charge transfer potential can be modified to address systems involving oxygen and numerous metal elements [23]. Here we parametrize such a modified charge transfer potential for the quinternary O–Al–Ni–Co–Fe system needed to study the growth of $Ni_xCo_yFe_{1-x-y}/AlO_x/Co_xFe_{1-x}$ multilayers [1, 2].

2. Charge transfer potentials for metal and metal oxide heterostructures

Simulations of metal and metal oxide heterostructures require an interatomic potential that is transferable from pure metal or pure oxygen local configurations where the ionic interactions are neglected to fully developed metal oxide regions where the ionic interactions are strong. Charge transfer potentials seek to achieve this by writing the total potential energy of the system, E, as a sum of non-ionic energy, E_N, and ionic energy, E_I:

$$E = E_N + E_I. \tag{1}$$

The ionic energy, E_I, depends on the charges on atoms. The charges on atoms dynamically vary depending on local environments. Equation (1) can be normalized such that E_I becomes zero when the charges on the atoms are zero. The non-ionic energy, E_N, can then be viewed simply as the potential energy of the pure metal or pure oxygen systems, and its transferability to oxide systems is addressed by the additional charge transfer ionic interaction, E_I, as the system is progressively ionized. A charge transfer potential for a metal and metal oxide heterostructure then requires two models to separately define E_N and E_I.

For the O–Al–Ni–Co–Fe system discussed here, the embedded atom method (EAM) potential originally proposed by Daw and Baskes [24] can be used for E_N, and a recently proposed charge transfer ionic model (CTIP) [23] provides an expression for E_I. Unlike earlier CTIP models [19, 20], which incorrectly predicted non-zero charges in pure metal alloy systems, the recent CTIP guarantees zero charges in any metallic systems. As a result, E_I drops to zero in a pure metal and the EAM + CTIP model for $E_N + E_I$ is essentially equivalent to the EAM model of E_N. This not only ensures the fidelity of the metal systems, but also allows us to independently parametrize E_N for the metal system of interest and then address the $E_N + E_I$ potential for its oxide system.

2.1. Non-ionic embedded atom method potential

The EAM potential originally proposed by Daw and Baskes [24] has been successfully used for modelling metals, especially the closely packed fcc metals. A unified EAM potential

database has recently been developed for a variety of metals, including most of those of interest in magnetic layers [16, 25]. This EAM potential database is based upon an alloy EAM model [26] and has been used to explore the atomic assembly mechanisms of vapour deposited metal multilayers [16–18]. The non-ionic potentials for the Al, Ni, Co, and Fe interactions are adapted from this EAM database.

In the EAM approach, the total energy for a system of N atoms is expressed as

$$E_{\mathrm{N}} = \tfrac{1}{2}\sum_{i=1}^{N}\sum_{j=i_1}^{i_N}\phi_{ij}(r_{ij}) + \sum_{i=1}^{N}F_i(\rho_i) \tag{2}$$

where $\phi_{ij}(r_{ij})$ is the pair energy between atoms i and j separated by a distance r_{ij}, $i_1, i_2, \ldots, i_N$ is a list of all neighbours of atom i, and F_i is the embedding energy arising from embedding an atom i into a local site with an electron density background ρ_i. If the cut-off distance of the potential is less than half of the periodic length of the computational cell, all neighbours of a given atom can be found in one computational cell; hence, no image atoms need to be considered. However, the formulism used here assumes no limit on the cut-off distance. As a result, atom j and many of its images can become the neighbours of atom i (even the images of i can be i's neighbours). Our list notation of $i_1, i_2, \ldots, i_N$ concisely represents this scenario because no additional periodic boundary conditions need to be considered as long as all of the image atoms are included in this list.

The generalized elemental pair potential is represented by

$$\phi(r) = \frac{A\exp[-\alpha(\frac{r}{r_{\mathrm{e}}}-1)]}{1+(\frac{r}{r_{\mathrm{e}}}-\kappa)^{20}} - \frac{B\exp[-\beta(\frac{r}{r_{\mathrm{e}}}-1)]}{1+(\frac{r}{r_{\mathrm{e}}}-\lambda)^{20}} \tag{3}$$

where r_{e} is the equilibrium spacing between nearest neighbour atoms in the elemental structure, and A, B, α, and β are four adjustable parameters. Note that as r increases the denominator of the right-hand side of equation (3) becomes very large. This provides a natural cut-off distance for the potential, which is controlled by parameters κ and λ.

The local electron density, ρ_i, can be calculated using

$$\rho_i = \sum_{j=i_1}^{i_N} f_j(r_{ij}) \tag{4}$$

where $f_j(r_{ij})$ is the electron density contribution from atom j at the site of atom i. The electron density function is expressed using the same form as the attractive part of the pair potential:

$$f(r) = \frac{f_{\mathrm{e}}\exp[-\beta(\frac{r}{r_{\mathrm{e}}}-1)]}{1+(\frac{r}{r_{\mathrm{e}}}-\lambda)^{20}} \tag{5}$$

where only f_{e} is an additional fitting parameter. To create an elemental metal embedding energy function that works well with a wide range of conditions, the embedding energy is defined by different expressions in different electron density ranges. These expressions are constrained to have matching values and slopes at their junctions. They are listed in the following equations:

$$F(\rho) = \sum_{i=0}^{3} F_{ni}\left(\frac{\rho}{\rho_n}-1\right)^i, \qquad \rho < \rho_n, \quad \rho_n = 0.85\rho_{\mathrm{e}} \tag{6}$$

$$F(\rho) = \sum_{i=0}^{3} F_i^{-}\left(\frac{\rho}{\rho_{\mathrm{e}}}-1\right)^i, \qquad \rho_n \leqslant \rho < \rho_{\mathrm{e}} \tag{7}$$

$$F(\rho) = \sum_{i=0}^{3} F_i^{+}\left(\frac{\rho}{\rho_{\mathrm{e}}}-1\right)^i, \qquad \rho_{\mathrm{e}} \leqslant \rho < \rho_o, \quad \rho_o = 1.15\rho_{\mathrm{e}} \tag{8}$$

$$F(\rho) = F_{\mathrm{e}}\left[1 - \ln\left(\frac{\rho}{\rho_s}\right)^{\eta}\right]\left(\frac{\rho}{\rho_s}\right)^{\eta}, \qquad \rho_o \leqslant \rho \tag{9}$$

where ρ_{e} is the electron density at the lattice site of the equilibrium elemental metal structure and ρ_s, F_{ni}, F_i^-, F_i^+ ($i = 0, 1, 2,$ or 3), F_{e}, and η are fitting parameters. Equations (2)–(9) sufficiently define the potentials for elemental metals.

For metal alloys, the only other functions needed are the pair cross potentials between different species a and b. Using the normalized alloy EAM model [26], the pair potential between two different species, a and b, can be constructed from their elemental potentials:

$$\phi_{ab}(r) = \frac{1}{2}\left[\frac{f_b(r)}{f_a(r)}\phi_{aa}(r) + \frac{f_a(r)}{f_b(r)}\phi_{bb}(r)\right]. \tag{10}$$

Equations (2)–(9) are used for the elemental functions of all the metal elements (Al, Ni, Co, and Fe) and the constructed pair cross potential of equation (10) for most pairs (Al–Co, Al–Fe, Ni–Co, Ni–Fe, and Co–Fe). While the pair cross potential of equation (10) is not directly fitted to the metal alloy properties, it gives reasonable values of heats of solution [27]. In the NiCoFe/AlO_x/NiCoFe MTJ multilayers, chemical composition close to that of the NiAl intermetallic compound may be encountered during the growth of aluminium on the $Ni_{0.65}Co_{0.20}Fe_{0.15}$ layer (prior to oxidation of the aluminium layer). To more realistically reflect this scenario, we have used equation (3) for the Al–Ni pair cross potential to fit it to the cohesive energy of the B2 phase of the NiAl intermetallic compound.

The general formula, equation (3), is also used to represent the elemental oxygen pair potential and all pair cross potentials between oxygen and the metals (O–Al, O–Ni, O–Co, and O–Fe). The electron density for oxygen was fitted using

$$f(r) = \frac{f_{\mathrm{e}}\exp[-\gamma(\frac{r}{r_{\mathrm{e}}} - 1)]}{1 + (\frac{r}{r_{\mathrm{e}}} - \nu)^{20}}. \tag{11}$$

Unlike equation (5), where β and λ are the same as those in the attractive part of the pair potential, equation (11) introduces two different parameters, γ and ν, to provide sufficient flexibility for the fitting of oxide properties.

With the potential parameters for the metals known, the remaining parameters for the oxygen–metal (Al, Ni, Co and Fe) system are derived using properties of the binary oxides involving Al, Ni, Co, and Fe, namely the corundum phase of Al_2O_3 and Fe_2O_3 and the B1 phase of CoO and NiO. These oxides define four different oxygen lattice sites, which correspond to four equilibrium electron densities, $\rho_{\mathrm{e},i}$ (where $i = 1, 2, 3,$ or 4). We arrange the four oxides so that $\rho_{\mathrm{e},1}$, $\rho_{\mathrm{e},2}$, $\rho_{\mathrm{e},3}$, and $\rho_{\mathrm{e},4}$ represent an increasing sequence of the electron densities and fit with a spline function. This ensures that the oxygen embedding energy function goes smoothly through the appropriate range of electron densities while correctly defining the structures, lattice constants, cohesive energies, and bulk moduli for each oxide. When all the other potential functions are given, the lattice constants, cohesive energy, and bulk modulus of an oxide i are determined by the oxygen embedding energy as well as its first and second derivatives, at least within a small electron density range near $\rho_{\mathrm{e},i}$, $\rho_{\min,i} \leqslant \rho < \rho_{\max,i}$, where $\rho_{\min,i} < \rho_{\mathrm{e},i}$ and $\rho_{\max,i} > \rho_{\mathrm{e},i}$. A quadratic spline function can be used to achieve this. A cubic spline can be used to extend the oxygen embedding energy to the lowest electron density range $\rho_{\min,0} \leqslant \rho < \rho_{\max,0}$, where $\rho_{\min,0} = 0$ and $\rho_{\max,0} = \rho_{\min,1}$. This results in cubic spline functions for the oxygen embedding energy of the form

$$F(\rho) = \sum_{i=0}^{3} F_{i,j}\left(\frac{\rho}{\rho_{\mathrm{e},j}} - 1\right)^i, \qquad \text{for } \rho_{\min,j} \leqslant \rho < \rho_{\max,j}, \quad j = 0, 1, 2, 3, 4. \tag{12}$$

In equation (12) $\rho_{e,j}$ ($j = 1, 2, 3,$ or 4) is the equilibrium electron density at the oxygen site of the jth oxide and $F_{i,j}$ ($i = 0, 1, 2,$ or 3 and $j = 0, 1, 2, 3,$ or 4) and $\rho_{e,0}$ are additional fitting parameters. Note that equation (12) is expressed in a general cubic function form. Quadratic splines for $j = 1, 2, 3,$ or 4 correspond to $F_{3,j} = 0$.

2.2. *Charge transfer ionic potential*

When a metal is oxidized, metal atoms lose electrons to become cations and oxygen atoms gain electrons to become anions. The ionic interactions between cations and anions of metal oxides have often been described as the Coulomb interactions assuming fixed charges on the cations and anions [28–33]. The approach can be easily implemented in efficient MD algorithms and has been widely used to study bulk oxides [33, 34]. However, this approach cannot be used for metal/metal oxide heterostructures. First, the fixed charge model can only be used to study cases where the entire system is in one oxidation state. During metal oxidation or the growth of a metal/metal oxide structure, numerous oxide states with different charges on atoms can exist in the system. Furthermore, the fixed charge model cannot ensure charge neutrality during the simulation of oxidation, during which the oxygen concentration within the system continuously increases. Second, metal oxidation simulation using the fixed charge model requires injection of charged oxygen ions into the surface. They are brought from the far field, where in reality the oxygen atoms would be neutral. The fixed charge model hence introduces significant extra Coulomb energy and overestimates the latent heat of oxygen condensation by more than 10 eV/atom [23]. This can significantly affect the predicted atomic assembly sequence (as has been shown, an adatom energy change of only 5 eV can completely change the atomic structures of vapour deposited metal films) [16, 17]. Finally, a fixed charge potential cannot be used to investigate the interface between a metal and its oxide where the potential must smoothly switch between one dominated by ionic interactions (in the oxide region) to one dominated by metallic interactions (in the metal region).

Charge transfer ionic potentials have been proposed by Rappe and Goddard [19] and Streitz and Mintmire [20]. Using the Streitz–Mintmire formulism [20], the total ionic energy, E_I, is expressed as

$$E_I = \sum_{i=1}^{N} \left(\chi_i q_i + \tfrac{1}{2} J_i q_i^2\right) + \tfrac{1}{2} \sum_{i=1}^{N} \sum_{j=i_1}^{i_N} C_{ij}(r_{ij}, q_i, q_j) \tag{13}$$

where χ_i is the electronegativity of atom i [20], J_i ($J_i > 0$) is referred to as an 'atomic hardness' [35] or a self-Coulomb repulsion [19], q_i is the charge on atom i, and $C_{ij}(r_{ij}, q_i, q_j)$ is the Coulomb energy between atoms i and j when separated by a distance r_{ij}. The first term on the right-hand side of equation (13) essentially describes the self-ionization energy of atoms. Under the system neutral condition, $\sum_{i=1}^{N} q_i = 0$, any increase in the magnitude of charges on ions always results in an increase in the self-ionization energy of single elemental systems. However, if opposite charges are induced between neighbouring atoms (as in metal oxides), then an increase in the magnitude of charges reduces the Coulomb energy between any neighbouring positive and negative charges. The trade-off between self-ionization energy and Coulomb energy then defines a set of equilibrium charges on atoms q_i ($i = 1, 2, \ldots,$ or N) that minimizes the total energy of equation (13) under the system neutral constraint of $\sum_{i=1}^{N} q_i = 0$. The equilibrium charges can always be dynamically solved during MD simulations [21, 22]. Replacing the fixed charges with this set of equilibrium charges then resolves the many problems of the fixed charge models discussed above.

Rather than assuming a point charge on an ion, i, a more realistic approach is to assume that the ion has a diffused electron density distribution, σ_i, which is dependent on the radial

distance, r, from its core. This can be written

$$\sigma_i(r, q_i) = Z_i\delta(r) + (q_i - Z_i)\frac{\xi_i^3}{\pi}\exp(-2\xi_i r) \tag{14}$$

where $\delta(r)$ is a delta function [$\delta(r) = 1$ at $r = 0$ and $\delta(r) = 0$ at $r \neq 0$], Z_i is an effective core charge (treated as a fitting parameter), and ξ_i is a parameter defining the spread of the electron distribution. Z_i satisfies the condition $0 \leqslant Z_i \leqslant N_i$, where N_i is the total nuclear charge of the atom. Since $\int \sigma_i(r)\,\mathrm{d}V = q_i$, equation (14) is a spatially distributed representation of a charge q_i. Using equation (14) to integrate the Coulomb interaction and substituting the results into equation (13) yields normalized ionic energy as [20, 23]

$$E_\mathrm{I} = \sum_{i=1}^{N} X_i q_i + \tfrac{1}{2}\sum_{i=1}^{N}\sum_{j=1}^{N} V_{ij}(r_{ij})q_i, q_j \tag{15}$$

where

$$X_i = \chi_i + k_\mathrm{c}\sum_{j=i_1}^{i_N} Z_j P_{ij}(r_{ij}), \tag{16}$$

and

$$V_{ij}(r_{ij}) = J_i\delta_{ij} + k_\mathrm{c}\sum_{k=i_1(j)}^{i_N(j)} Q_{ik}(r_{ik}). \tag{17}$$

Here for $\xi_i = \xi_j = \xi$

$$P_{ij}(r) = \left(\tfrac{3}{8}\xi + \tfrac{3}{4}\xi^2 r + \tfrac{1}{6}\xi^3 r^2\right)\exp(-2\xi r) \tag{18}$$

$$Q_{ik}(r) = \frac{1}{r} - \frac{1}{r}\left(1 + \frac{11}{8}\xi r + \frac{3}{4}\xi^2 r^2 + \frac{1}{6}\xi^3 r^3\right)\exp(-2\xi r) \tag{19}$$

and for $\xi_i \neq \xi_j$

$$\begin{aligned} P_{ij}(r) = &-\left(\xi_i + \frac{1}{r}\right)\exp(-2\xi_i r) + \frac{\xi_i\xi_j^4\exp(-2\xi_i r)}{(\xi_i + \xi_j)^2(\xi_i - \xi_j)^2} + \frac{\xi_j\xi_i^4\exp(-2\xi_j r)}{(\xi_j + \xi_i)^2(\xi_j - \xi_i)^2} \\ &+ \frac{(3\xi_i^2\xi_j^4 - \xi_j^6)\exp(-2\xi_i r)}{r(\xi_i + \xi_j)^3(\xi_i - \xi_j)^3} + \frac{(3\xi_j^2\xi_i^4 - \xi_i^6)\exp(-2\xi_j r)}{r(\xi_j + \xi_i)^3(\xi_j - \xi_i)^3} \end{aligned} \tag{20}$$

$$\begin{aligned} Q_{ik}(r) = &\frac{1}{r} - \frac{\xi_i\xi_j^4\exp(-2\xi_i r)}{(\xi_i + \xi_j)^2(\xi_i - \xi_j)^2} - \frac{\xi_j\xi_i^4\exp(-2\xi_j r)}{(\xi_j + \xi_i)^2(\xi_j - \xi_i)^2} \\ &- \frac{(3\xi_i^2\xi_j^4 - \xi_j^6)\exp(-2\xi_i r)}{r(\xi_i + \xi_j)^3(\xi_i - \xi_j)^3} - \frac{(3\xi_j^2\xi_i^4 - \xi_i^6)\exp(-2\xi_j r)}{r(\xi_j + \xi_i)^3(\xi_j - \xi_i)^3}. \end{aligned} \tag{21}$$

In equations (16) and (17), $k_\mathrm{c} = 14.4$ eV Å e^{-2} is the Coulomb constant (e represents the electron charge), $\delta_{ij} = 1$ when $i = j$ and $\delta_{ij} = 0$ when $i \neq j$, and the notation $i_1(j), i_2(j), \ldots, i_N(j)$ means all the j atoms (i.e., j and its images) that are within the cut-off distance of atom i.

$V_{ij}(r_{ij})$ defined in equations (17), (19), and (21) involves a summation of $1/r_{ij}$. The direct summation of the slowly decaying function $1/r$ imposes a serious divergence problem. Note that the total contribution of these divergent terms to the system energy is $\frac{1}{2}\sum_{i=1}^{N}\sum_{j=i_1}^{i_N}\frac{q_i q_j}{r_{ij}}$. It can be replaced by fast convergent Ewald summations [23, 36, 37] under the system neutral condition. The Ewald approach was therefore used to modify V_{ij} to eliminate the divergence problem.

Equation (15) is a function of both atom positions and atom charges. During simulations, charges are dynamically solved from the energy minimization conditions at each time step. Once charges are known, equation (15) becomes a function of atom positions only. Because charges are solved from energy minimization conditions, their derivatives have no effects on forces or stresses. Equation (15) can then be used to calculate forces and stresses as if the charges were constant.

The Streitz–Mintmire CTIP model, equation (15), has been combined with an EAM potential for non-ionic interactions to study a binary Al–O system [20]. This Al–O potential was used in MD to simulate the oxidation of aluminium surfaces [21, 22]. However, this CTIP model has been found to have two problems.

To illustrate the first problem, consider a simple system containing only a positive point charge and a negative point charge. According to equation (13), the ionic energy can be written

$$E_{\mathrm{I}} = \chi_1 q_1 + \chi_2 q_2 + \frac{1}{2} J_1 q_1^2 + \frac{1}{2} J_2 q_2^2 + k_{\mathrm{c}} \frac{q_1 q_2}{r_{12}}. \tag{22}$$

Under the system neutral condition, $q_1 = -q_2$, equation (22) becomes

$$E_{\mathrm{I}} = (\chi_1 - \chi_2) q_1 + \left(\frac{J_1 + J_2}{2} - \frac{k_{\mathrm{c}}}{r_{12}} \right) q_1^2. \tag{23}$$

It can be seen that equation (23) only has a minimum when $\frac{J_1+J_2}{2} - \frac{k_{\mathrm{c}}}{r_{12}} > 0$ (i.e., a concave parabolic curve). To ensure the existence of the energy minimum and well defined equilibrium charges, the spacing between the atoms must be larger than a critical value $r_{\mathrm{c}} = \frac{2k_{\mathrm{c}}}{J_1+J_2}$. When this is not satisfied, equation (23) ceases to have a minimum (it becomes a convex parabolic curve), and E_{I} continues to decrease as the magnitude of charge increases. This results in infinitely large magnitudes of charges and overflow of the simulations. This effect occurs because the Coulomb interaction incorrectly overpowers the self-ionization energy in equation (22) at a short atomic spacing. In earlier applications of CTIP models [20–22], the problem was implicitly overcome. First, the short range repulsion in non-ionic potentials was formulated to prevent the atomic spacing from becoming too small. Second, the CTIP parameters, such as J_1 and J_2, were chosen to be reasonably large so that they defined a small r_{c}. In fact, we discovered that the original CTIP model and parametrizations for the Al–O system [20] were always unstable and always caused calculation overflow when combined with a standard EAM potential for Zr and Al [16, 25] to simulate ZrO_2 or Al_2O_3 surfaces. The constraints imposed by the original CTIP model upon the model parameters were not physical and prevented merging of the CTIP with the metal alloy EAM potential database [16, 25].

In addition, the original charge transfer model can only be used to study oxygen–single-metal (binary) systems. The non-ionic potential, E_{N}, must fully describe the potential for any non-ionized part of the systems (such as metal elements and metal alloys). In order for the full charge transfer CTIP + EAM potential to be equivalent to the EAM potential of metals, $E_{\mathrm{N}} + E_{\mathrm{I}}$ must reduce to E_{N} in metals. Equation (15) indicates that $E_{\mathrm{I}} = 0$ when all the charges, q_i, become zero. This means that the CTIP model gives correct energy as long as it correctly predicts zero charges in any metal systems. Note here that metal alloys can have minor charges from first principles. This charge contribution, however, has already been incorporated in EAM and the zero charges are required to comply with the notion that EAM fully describes metal systems.

The Streitz–Mintmire original CTIP model yielded zero charges for aluminium atoms in either bulk aluminium or a local aluminium region of the Al/AlO_x multilayers [20, 23]. However, this was achieved only when a single metal was involved. To illustrate, consider

again the simple pair of point charges. Setting the first derivative of E_I with respect to q_1 equal to zero, equation (23) yields

$$q_1 = \frac{(\chi_2 - \chi_1)r_{12}}{(J_1 + J_2)r_{12} - 2k_c}. \tag{24}$$

Equation (24) gives a zero charge, q_1, only when χ_1 and χ_2 are identical (i.e., 1 and 2 are of the same species). This is because when all atoms have the same charge properties no atoms have a preference to become positive charges on introducing negative charges to their neighbours. In metal alloys, however, neighbouring metal atoms can be different species (with different charge parameters). As a result, the original CTIP model predicts incorrectly non-zero charges in unoxidized metal alloy regions. A physical method to ensure a zero charge in metal alloys needs to be developed in order for the model to be used in systems involving more than one metal element.

A modified CTIP model has been proposed to resolve both problems of the earlier CTIP models [23]. It was based on the incorporation of the notion that the charge on an atom must be bounded by its valence. The ionic potential, equation (15), is then modified by the addition of two charge constraining energy terms:

$$E_I = \sum_{i=1}^{N} X_i q_i + \tfrac{1}{2}\sum_{i=1}^{N}\sum_{j=1}^{N} V_{ij}(r_{ij}) q_i \cdot q_j + \sum_{i=1}^{N} \omega S[-(q_i - q_{i,\min})](q_i - q_{i,\min})^2 + \sum_{i=1}^{N} \omega S(q_i - q_{i,\max})(q_i - q_{i,\max})^2 \tag{25}$$

where $S(x)$ is a step function [$S(x) = 0$ when $x \leqslant 0$ and $S(x) = 1$ when $x > 0$], $q_{i,\min}$ and $q_{i,\max}$ are boundaries for charge q_i, and ω is a constant. It can be seen that when charge q_i is within the boundaries, $q_{i,\min} \leqslant q_i \leqslant q_{i,\max}$, equation (25) is equivalent to equation (15). However, when the charge falls out of this range, an additional energy penalty is imposed. The magnitude of the energy penalty can be controlled by parameter ω. By setting the charge boundaries of metal atoms between zero and the maximum number of their valence electrons, and the charge boundaries of oxygen atoms between -2 and 0, an energy minimization of equation (25) with a relatively large value of ω can ensure that metal atoms only lose electrons until all of their outer shell electrons are transferred while oxygen atoms only acquire electrons until their outer shell is completely filled. With equation (25), the critical atomic spacing for the occurrence of calculation instability becomes $r_c = \frac{2k_c}{J_1+J_2+4\omega}$ [23]. A moderate value of $\omega = 40.0$ produces an $r_c = 0.18$ Å, even at $J_1 = J_2 = 0$ where the old CTIP model would predict $r_c = \infty$ [23]. As a result, stable simulations are guaranteed under any conditions for any choice of CTIP model parameters. This occurs because the charge boundary constraining energy terms overpower the Coulomb energy through imposition of valence. It should be noted that ω has a physical meaning and can be determined by first principle calculations. However, its precise value is not needed here because the only effect ω has is to set up the charge boundaries, and any ω value above 20 leads to essentially the same result.

Equation (25) ensures that metal atoms can only have positive charges and oxygen atoms can only have negative charges. It then naturally results in zero charges in pure metal systems. Consider, as an example, a pair of aluminium and nickel atoms. Assume that the aluminium atom seeks to become a positive charge by inducing a negative charge on the nickel atom. The nickel atom, however, cannot be negatively charged because it is set to be in the positive charge range. This would force a zero charge on the nickel atom. The aluminium atom, on the other hand, cannot become positively charged because it does not have an anion to interact with (note that in this simple case the system neutrality requirement also forces a zero aluminium

Table 1. EAM parameters for metals.

Metal	r_e (Å)	f_e	ρ_e	ρ_s	α	β	A (eV)
Al	2.863 92	1.203 78	17.517 47	19.900 41	6.613 17	3.527 02	0.314 87
Ni	2.488 75	2.211 49	30.370 03	30.371 37	8.383 45	4.471 17	0.429 05
Co	2.505 98	2.315 44	31.891 66	31.891 66	8.679 63	4.629 13	0.421 38
Fe	2.481 99	2.314 53	24.595 73	24.595 73	9.818 27	5.236 41	0.392 81
Metal	B (eV)	κ	λ	F_{n0} (eV)	F_{n1} (eV)	F_{n2} (eV)	F_{n3} (eV)
Al	0.365 55	0.379 85	0.759 69	−2.807 60	−0.301 44	1.258 56	−1.247 60
Ni	0.633 53	0.443 60	0.820 66	−2.693 51	−0.076 44	0.241 44	−2.375 63
Co	0.640 11	0.500 00	1.000 00	−2.541 80	−0.219 42	0.733 38	−1.589 01
Fe	0.646 24	0.170 31	0.340 61	−2.534 99	−0.059 60	0.193 06	−2.282 32
Metal	F_0 (eV)	F_1 (eV)	F_2 (eV)	F_3^- (eV)	F_3^+ (eV)	η (eV)	F_e (eV)
Al	−2.83	0.0	0.622 25	−2.488 24	−2.488 24	0.785 91	−2.824 53
Ni	−2.70	0.0	0.265 39	−0.152 86	4.585 68	1.013 18	−2.708 39
Co	−2.56	0.0	0.705 85	−0.687 14	3.092 13	1.077 02	−2.565 84
Fe	−2.54	0.0	0.200 27	−0.148 77	6.694 65	1.182 90	−2.551 87
Pair	r_e (Å)	α	β	A (eV)	B (eV)	κ	λ
Al–Ni	2.715 79	8.004 43	4.759 70	0.442 54	0.683 49	0.632 79	0.817 77

charge). Since zero charges are guaranteed, the CTIP potential can be superimposed on any EAM potential so that the full CTIP + EAM potential is transferable to the EAM potential when used for a metal or metal alloy system.

Equation (25) is a quadratic type of potential with respect to q_i. It has been demonstrated that the minimum ionic energy and the equilibrium charges defined by equation (25) for a neutral system ($\sum_{i=1}^{N} q_i = 0$) can be effectively solved using an integrated conjugate gradient technique and a Newton–Raphson method [23].

3. Parametrization

A relatively long cut-off distance of 12 Å was used for the potential. This cut-off distance addresses the long range Coulomb interactions relatively well. It does not affect the properties of the existing EAM potential [16, 25] because equations (3) and (5) enable the potential to be virtually cut off at 7 Å or below.

Since the modified CTIP model has no effect on the potential that describes the metal system, the existing EAM potential database [16, 25] can in principle be used directly for metal alloys. To better fit the oxide properties, however, we have rescaled f_e and ρ_e by a common factor and slightly adjusted the third derivative of the embedding energy at the equilibrium electron density and the corresponding splined functions. Because only the third derivative is modified and the embedding energy is expressed as a function of relative electron density rather than absolute value (see equations (6)–(9)), the modified EAM potentials do not change the cohesive energy, vacancy formation energy, lattice constants, and elastic constants predicted by the old parameters [16, 25]. The revised EAM parameters for the metals of interest here are shown in table 1.

Instead of using the alloy EAM model, equation (10), the pair cross potential between aluminium and nickel was fitted to the experimental cohesive energy of the B2 phase of NiAl using equation (3). All of the fitted EAM parameters for the metals are summarized in table 1.

Table 2. CTIP parameters for all elements.

Element	$q_{\min}$ (e)	$q_{\max}$ (e)	χ (eV e^{-1})	J (eV e^{-2})	ξ (Å^{-1})	Z (e)
O	−2	0	2.000 00	14.995 23	2.144	0.000 00
Al	0	3	−1.479 14	9.072 22	0.968	1.075 14
Ni	0	2	−1.708 04	9.109 54	1.087	1.444 50
Co	0	2	−1.677 65	8.657 73	1.055	1.544 98
Fe	0	3	−1.905 87	8.998 19	1.024	1.286 12

Table 3. Parameters for EAM pair potentials between oxygen and oxygen as well as oxygen and all other metals.

Pair	r_e (Å)	α	β	A (eV)	B (eV)	κ	λ
O–O	3.648 57	5.440 72	3.597 46	0.349 00	0.574 38	0.080 07	0.393 10
O–Al	2.985 20	8.497 41	4.521 14	0.097 38	0.381 21	0.189 67	0.952 34
O–Ni	2.957 32	7.965 28	4.424 11	0.135 21	0.253 32	0.470 77	0.655 24
O–Co	2.595 86	8.252 24	4.375 48	0.257 14	0.340 29	0.374 19	0.508 43
O–Fe	3.079 92	7.523 09	4.133 30	0.171 08	0.398 69	0.223 35	0.343 80

Table 4. EAM parameters for oxygen electron density function.

f_e	γ	ν
1.394 78	2.117 25	0.374 57

With the metal EAM potentials determined, all of the other parameters were fitted to give optimum predictions of the experimental cohesive energies, lattice constants, elastic constants, and crystal structures of the four binary metal oxides: corundum Al_2O_3 and Fe_2O_3, and B1 CoO and NiO. First, the charge bounds, $q_{\min,i}$ and $q_{\max,i}$, were chosen to match the valences of all species, table 2. To set these charge bounds, we used a value of $\omega = 20$. The charge parameter, ξ, characterizes the spread distance of the charge, which was taken to be inversely proportional to the atomic radius. To be consistent with earlier work [23], we fitted the other charge parameters under the constraint that the anion charge in all four equilibrium bulk oxides is −1.933.

To construct the oxygen embedding energy function, the electron density range for the splined function of each oxide was chosen as $\rho_{\min,i} = 0.5(\rho_{e,i-1} + \rho_{e,i})$ for $i = 2$, 3, or 4 and $\rho_{\max,i} = 0.5(\rho_{e,i} + \rho_{e,i+1})$ for $i = 1$, 2, or 3. Only $\rho_{\min,1}$ and $\rho_{\max,4}$ are not defined. We then took $\rho_{\min,1}$ as $0.85\rho_{e,1}$ and $\rho_{\max,4}$ as ∞. Finally, we chose $\rho_{\min,0} = 0$ and $\rho_{\max,0} = \rho_{\min,1}$ to extrapolate the embedding energy function from $\rho_{\min,1}$ to zero electron density.

Using the constraints discussed above, a conjugate gradient method was used to fit all of the remaining model parameters. The fitting included three minimizations: the minimization of deviation of the predicted cohesive energies, lattice constants, and single-crystal elastic constants of the four oxides from those of experimental values; the minimization of forces on atoms and stresses on the bulk oxides to ensure the correct lattice constants and stability of crystals; and the minimization of the differences of the oxygen embedding energy and its derivatives at each splined junction to yield a smooth oxygen embedding energy function. The fitted parameters deduced by this procedure are listed in table 2 for all of the charge parameters, table 3 for the EAM pair potentials between oxygen and oxygen as well as oxygen and all other metals, table 4 for the oxygen electron density, and table 5 for the splined oxygen embedding energy function.

Table 5. EAM parameters for the splined oxygen embedding energy function.

i	$F_{0,i}$ (eV)	$F_{1,i}$ (eV)	$F_{2,i}$ (eV)	$F_{3,i}$ (eV)	$\rho_{e,i}$	$\rho_{\min,i}$	$\rho_{\max,i}$
0	−1.564 89	−1.391 23	1.771 99	1.598 33	54.629 10	0	54.629 10
1	−1.589 67	1.306 36	9.810 33	0.000 00	64.269 53	54.629 10	65.240 78
2	−1.541 16	2.028 21	6.562 40	0.000 00	66.212 02	65.240 78	66.567 97
3	−1.517 98	2.309 79	7.695 82	0.000 00	66.923 91	66.567 97	70.577 48
4	−1.190 82	4.129 36	10.323 38	0.000 00	74.231 05	70.577 48	∞

Table 6. Elemental and compound metal properties predicted by the metal EAM potentials.

Elements or compounds		Al	Ni	Co	Fe	NiAl
Structure		fcc	fcc	hcp	bcc	B2
Lattice constants (Å)	a	4.05	3.52	2.51	2.87	2.99
	c	—	—	4.08	—	—
Cohesive energy (eV)		3.58	4.45	4.41	4.29	4.32
Vacancy formation energy (eV)		0.65	1.68	1.82	1.65	—
Elastic constants (eV Å^{-3})	C_{11}	0.67	1.54	1.83	1.43	0.56
	C_{12}	0.38	0.92	0.86	0.85	0.85
	C_{13}	0.38	0.92	0.79	0.85	0.85
	C_{14}	0.00	0.00	0.00	0.00	0.00
	C_{33}	0.67	1.54	2.29	1.43	0.56
	C_{44}	0.18	0.78	0.40	0.73	0.46
	C_{66}	0.18	0.78	0.48	0.73	0.46

4. Characteristics of the CTIP + EAM potential

We have plotted the components of the EAM potentials in figures 1–3. The EAM metal potentials [16, 25] were well fitted to the elemental cohesive energies, vacancy formation energies, lattice constants, and elastic constants. Table 6 shows metal properties predicted by the potentials.

In our parametrization, the model predictions of the metal oxide properties were optimized to the reference values while the previously fitted metal properties were not affected. The oxide properties predicted by the optimized potentials are compared in table 7 with the reference values. Here, the experimental cohesive energies [16, 25, 38, 39], lattice constants [40, 41], and elastic constants [39, 41] were used as the reference values. It can be seen from table 7 that the predicted cohesive energies and lattice constants are precise while the elastic constants are in reasonable agreement with the experimental values.

To examine the responses of charge on atoms to the environment, the CTIP model was used to calculate the charge as a function of isotropic lattice strain for the four oxides. Results for the anion charges are plotted in figure 4. It indicates that charge decreases as the lattices are pulled apart. Unlike the original CTIP model where charge becomes unstable when the lattice is highly compressed [23], the anion charge calculated here was bounded to approximately $-2e$ even when the lattice was compressed to a hydrostatic strain of -0.3.

The cohesive energies of the four oxides were also calculated as a function of hydrostatic strain from -0.3 to 1.0, and the results are plotted in figure 5. No instability problems occurred when the lattice was highly compressed. Reasonable energy versus strain curves were obtained over a wide range of strains.

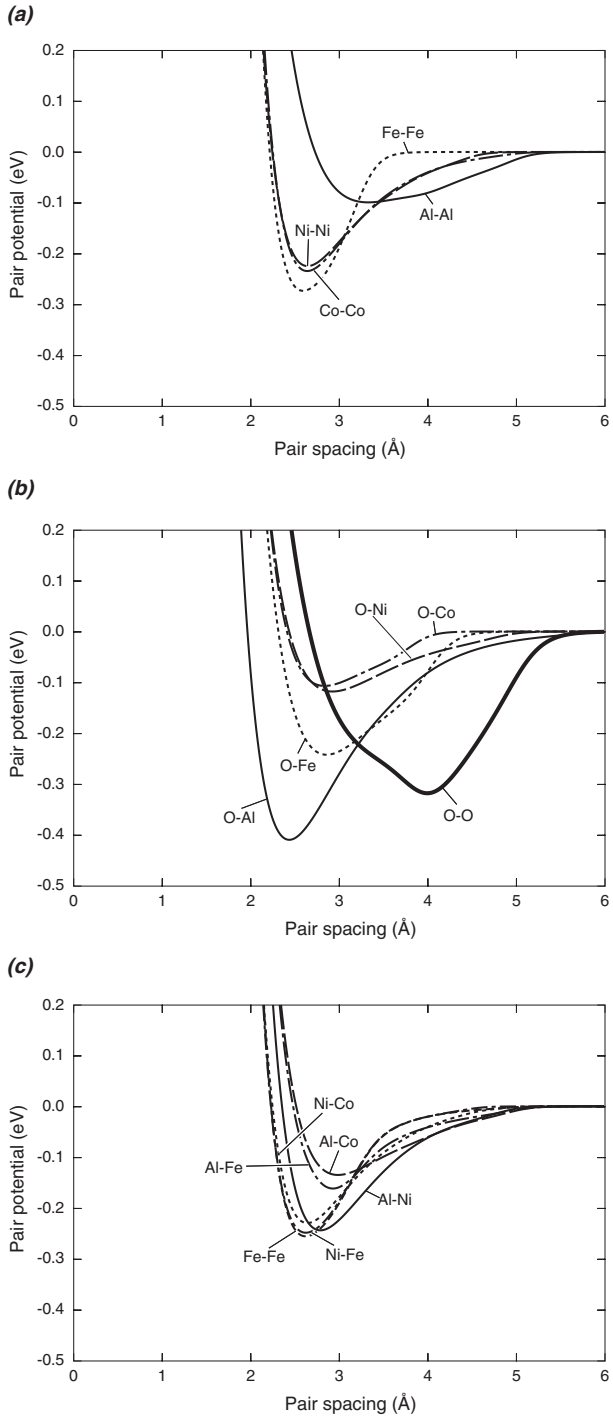

Figure 1. Characteristics of the EAM pair potentials: (a) elemental metal pair potentials; (b) oxygen–metal and oxygen–oxygen pair potentials; and (c) metal pair cross potentials.

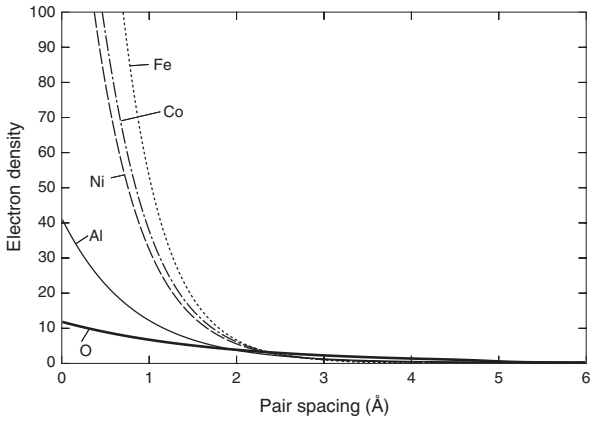

Figure 2. Characteristics of the EAM electron density functions.

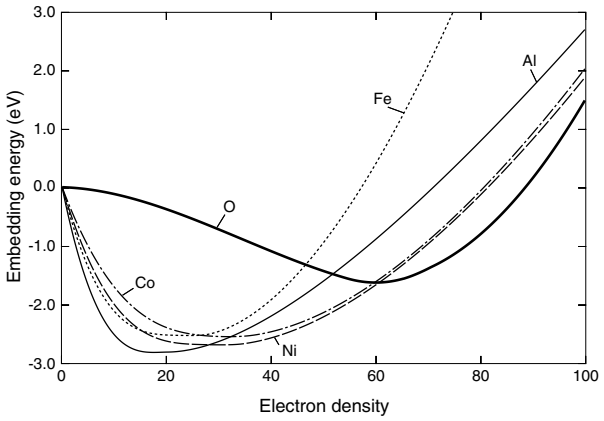

Figure 3. Characteristics of the EAM embedding energy functions.

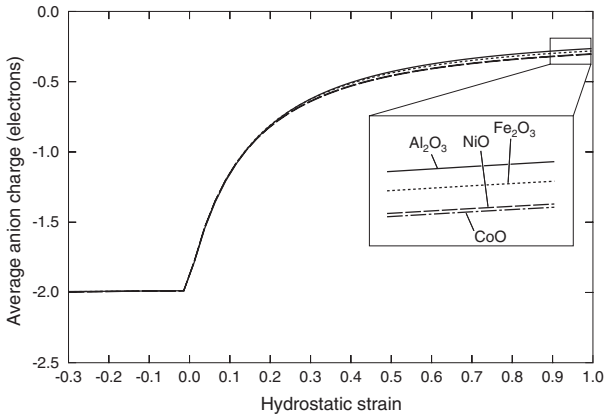

Figure 4. Average anion charge as a function of the hydrostatic strain for the four oxides: the corundum phase of Al_2O_3 and Fe_2O_3, and the B1 phase of CoO and NiO.

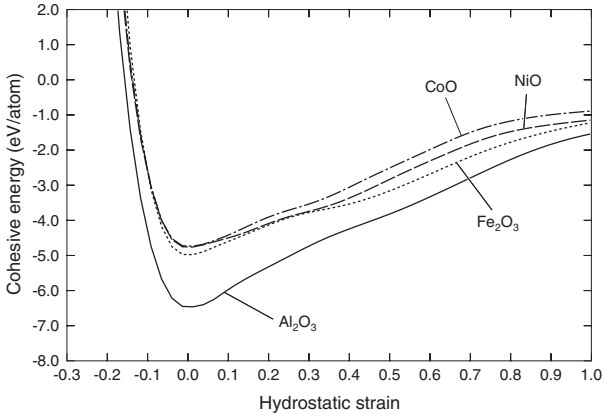

Figure 5. Cohesive energy as a function of the hydrostatic strain for the four oxides: the corundum phase of Al_2O_3 and Fe_2O_3, and the B1 phase of CoO and NiO.

Table 7. Calculated and experimental properties of oxides.

Oxides			Al_2O_3	Fe_2O_3	NiO	CoO
Structure			Corundum	Corundum	B1	B1
Lattice constants (Å)	a	Cal.	4.759	5.025	4.168	4.258
		Exp.	4.759	5.025	4.168	4.258
	c	Cal.	12.991	13.735	—	—
		Exp.	12.991	13.735	—	—
Cohesive energy (eV/formula)		Cal.	−6.461	−4.978	−4.762	−4.733
		Exp.	−6.461	−4.978	−4.762	−4.733
Elastic constants (eV Å^{-3})	C_{11}	Cal.	3.065	1.513	1.413	1.571
		Exp.	3.108	1.515	1.319	1.633
	C_{12}	Cal.	0.653	0.191	0.709	0.950
		Exp.	1.025	0.342	0.756	0.919
	C_{13}	Cal.	0.842	0.114	0.709	0.950
		Exp.	0.701	0.096	0.756	0.919
	C_{14}	Cal.	−0.168	−0.179	0.000	0.000
		Exp.	−0.147	−0.078	0.000	0.000
	C_{33}	Cal.	3.387	1.657	1.413	1.571
		Exp.	3.119	1.421	1.319	1.633
	C_{44}	Cal.	0.818	0.502	0.749	0.500
		Exp.	0.921	0.536	0.681	0.519
	C_{66}	Cal.	1.206	0.661	0.749	0.500
		Exp.	1.042	0.587	0.681	0.519

5. Illustrative simulation

We now demonstrate that the CTIP + EAM potential can be used to simulate the growth of metal/metal oxide multilayers using an MD method [16–18]. An fcc $Ni_{0.65}Co_{0.20}Fe_{0.15}$ crystal containing 120 $(22\bar{4})$ planes in the x direction, three (111) planes in the y direction, and 16 $(2\bar{2}0)$ planes in the z direction was created as the initial substrate. Under periodic boundary conditions in the x and z directions and a free boundary condition in the y direction, about six monolayers of $Ni_{0.65}Co_{0.20}Fe_{0.15}$ were first deposited on the (111) substrate surface using an

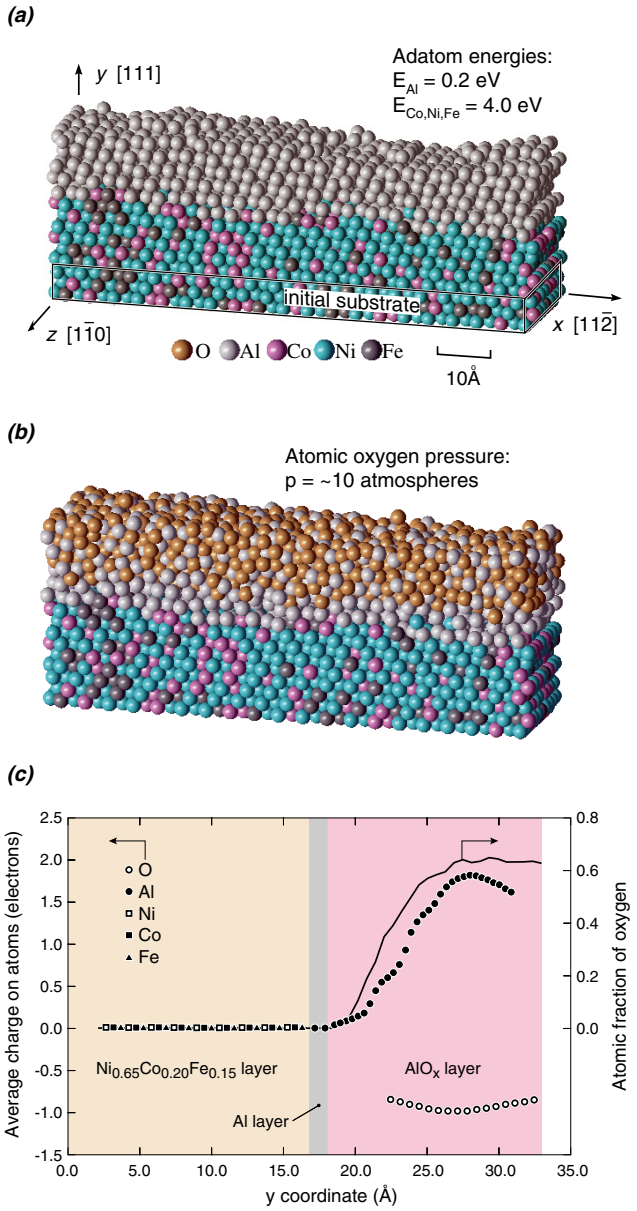

Figure 6. Simulated oxidation of Al/$Ni_{0.65}Co_{0.20}Fe_{0.15}$ metal multilayers: (a) vapour deposited Al-on-$Ni_{0.65}Co_{0.20}Fe_{0.15}$ metal multilayers prior to oxidation; (b) after oxidation; and (c) charges and oxygen concentration as a function of position across a multilayer interface.

adatom energy of 4.0 eV, a normal adatom incident angle, a substrate temperature of 300 K, and an accelerated deposition rate of 2 nm ns^{-1}. Another six aluminium monolayers were subsequently deposited under the same conditions except for a lower adatom energy of 0.2 eV. The resultant Al-on-$Ni_{0.65}Co_{0.20}Fe_{0.15}$ surface is shown in figure 6(a). Oxidation of the Al-on-$Ni_{0.65}Co_{0.20}Fe_{0.15}$ surface was then simulated by exposing the crystal to a highly reactive atomic oxygen vapour. An oxygen vapour temperature of 300 K and an oxygen atom vapour

density of 0.0003 atoms $Å^{-3}$ (corresponding to a pressure of approximately 10 atm) were used. The abnormally high oxygen pressure accelerated the oxidation so that sufficient oxide formed during the short timescale of the simulation. The charge was solved every 0.1 ps. The simulated atomic structure of the crystal after 290 ps of oxidation is shown in figure 6(b). It shows the formation of an aluminium oxide layer.

The CTIP + EAM potential should predict zero charges in local metal regions and significant charges in oxide regions. To investigate this, the average charges on Al, Ni, Co, Fe, and O atoms were calculated as a function of position across the simulated metal/metal oxide interface and the results are shown in figure 6(c). The oxygen concentration as a function of position along the crystal thickness direction is also superimposed in figure 6(c).

Figure 6(b) shows a successful direct MD simulation of the oxidation of a metal surface that involves four different metal elements. An amorphous surface AlO_x layer formed at the low temperature, which is in good agreement with experiments. It can be seen from figure 6(c) that the CTIP model predicted zero charge in the interior of the $Ni_{0.65}Co_{0.20}Fe_{0.15}$ alloy. Towards the surface where the AlO_x oxide formed, the aluminium charges rise until they approach a value of +2 while oxygen charges reduce until they approach a value of -1. The large magnitudes of charges correspond very well to regions where the oxygen concentration is significant. The results shown in figures 4–6 demonstrate that the CTIP + EAM model has captured much of the physics and chemistry needed to simulate the oxidation of the metallic alloys.

6. Conclusions

EAM potentials have long been used for atomistic simulations of metal and metal alloy systems. Here we have coupled a modified charge transfer ionic potential with existing embedded atom method potentials and propose a set of parameters for study of the O–Al–Ni–Co–Fe quinternary system. The potential parameters are optimized to accurately predict the cohesive energies, lattice constants, elastic constants, and crystal structures of the four binary oxides: the corundum phase of Al_2O_3, Fe_2O_3, and the B1 phase of CoO and NiO. The potential predicts physically realistic charges and lattice cohesive energies over a wide range of lattice strain. We have also showed that the dynamics of oxidation of an Al-on-$Ni_{0.65}Co_{0.20}Fe_{0.15}$ metal surface can be simulated by an MD method using this potential. The modified charge transfer ionic potential successfully predicted zero charges in the interior of the metal alloy region and large magnitudes of charge in the interior of the metal oxide. This potential appears to be well suited for studies of atomic assembly during magnetic tunnel junction growth by vapour deposition processes.

Acknowledgments

We thank Dr Stuart Wolf for helpful discussions of this work and acknowledge the support of the research by the Defense Advanced Research Projects Agency and the Office of Naval Research (C Schwartz and J Christodoulou, Program Managers) under grant N00014-03-C-0288.

References

[1] Beech R S, Anderson J, Daughton J, Everitt B A and Wang D 1996 *IEEE Trans. Magn.* **32** 4713
[2] Tondra M, Daughton J M, Wang D, Beech R S, Fink A and Taylor J A 1998 *J. Appl. Phys.* **83** 6688
[3] Moodera J S, Kinder L R, Wong T M and Meservey R 1995 *Phys. Rev. Lett.* **74** 3273
[4] Julliere M 1975 *Phys. Lett.* A **54** 225

[5] Durlam M, Naji P J, Omair A, DeHerrera M, Calder J, Slaughter J M, Engel B N, Rizzo N D, Grynkewich G, Butcher B, Tracy C, Smith K, Kyler K W, Ren J J, Molla J A, Feil W A, Williams R G and Tehrani S 2003 *IEEE J. Solid-State Circuits* **38** 796
[6] Zhu X and Zhu J G 2003 *IEEE Trans. Magn.* **39** 2854
[7] Prinz G A 1998 *Science* **282** 1660
[8] Nakatani R and Kitada M 1991 *J. Mater. Sci. Lett.* **10** 827
[9] Moodera J S, Nassar J and Mahon G 1999 *Annu. Rev. Mater. Sci.* **29** 381
[10] Shimazawa K, Sun J J, Kasahara N, Sato K, Kagami T, Saruki S, Redon O, Fujita Y, Umehara T, Syoji J, Araki S and Matsuzaki M 2001 *IEEE Trans. Magn.* **37** 1684
[11] van den Berg H A M, Altmann J, Bar L, Gieres G, Kinder R, Rupp R, Vieth M and Wecker J 1999 *IEEE Trans. Magn.* **35** 2892
[12] Motsnyi V F, de Boeck J, Das J, Roy W V, Borghs G, Goovaerts E and Safarov V I 2002 *Appl. Phys. Lett.* **81** 265
[13] Wolf S A, Awschalom D D, Buhrman R A, Daughton J M, von Molnar S, Roukes M L, Chtchelkanova A Y and Treger D M 2001 *Science* **294** 1488
[14] Zhu W, Hirschmugl C J, Laine A D, Sinkovic B and Parkin S S P 2001 *Appl. Phys. Lett.* **78** 3103
[15] Moodera J S, Gallagher E F, Robinson K and Nowak J 1997 *Appl. Phys. Lett.* **70** 3050
[16] Zhou X W, Wadley H N G, Johnson R A, Larson D J, Tabat N, Cerezo A, Petford-Long A K, Smith G D W, Clifton P H, Martens R L and Kelly T F 2001 *Acta Mater.* **49** 4005
[17] Zhou X W and Wadley H N G 1998 *J. Appl. Phys.* **84** 2301
[18] Zou W, Wadley H N G, Zhou X W and Johnson R A 2001 *Phys. Rev.* B **64** 174418
[19] Rappe A K and Goddard W A 1991 *J. Phys. Chem.* **95** 3358
[20] Streitz F H and Mintmire J W 1994 *Phys. Rev.* B **50** 11996
[21] Campbell T, Kalia R K, Nakano A, Vashishta P, Ogata S and Rodgers S 1999 *Phys. Rev. Lett.* **82** 4866
[22] Ogata S and Campbell T J 1998 *J. Phys.: Condens. Matter* **10** 11449
[23] Zhou X W, Wadley H N G, Filhol J-S and Neurock M N 2004 *Phys. Rev.* B **69** 35402
[24] Daw M S and Baskes M I 1984 *Phys. Rev.* B **29** 6443
[25] Zhou X W, Johnson R A and Wadley H N G 2004 *Phys. Rev.* B **69** 144113
[26] Johnson R A 1989 *Phys. Rev.* B **39** 12554
[27] Zhou X W and Wadley H N G 2004 *Phil. Mag.* **84** 193
[28] Baudin M and Hermansson K 2001 *Surf. Sci.* **474** 107
[29] Dick B G and Overhauser A W 1958 *Phys. Rev.* **112** 90
[30] Dwivedi A and Cormack A N 1990 *Phil. Mag.* A **61** 1
[31] Lindan P J D and Gillan M J 1993 *J. Phys.: Condens. Matter* **5** 1019
[32] Lewis G V and Catlow C R A 1985 *J. Phys. C: Solid State Phys.* **18** 1149
[33] Khan M S, Islam M S and Bates D R 1998 *J. Mater. Chem.* **8** 2299
[34] Catlow C R A 1990 *J. Chem. Soc. Faraday Trans.* **86** 1167
[35] Parr R G and Pearson R G 1983 *J. Am. Chem. Soc.* **105** 7512
[36] Parry D E 1975 *Surf. Sci.* **49** 433
[37] Heyes D M 1993 *Surf. Sci. Lett.* **293** L857
[38] Barin I 1989 *Thermochemical Data of Pure Substances* (Cambridge: VCH)
[39] *CRC Handbook of Chemistry and Physics* 1978 (Boca Raton, FL: CRC Press)
[40] Donnay J D H *et al* (ed) 1973 *Crystal Data, Determinative Tables* 3rd edn, vol II *Inorganic Compounds* (Swarthmore, PA: JCPDS-International Center for Diffraction Data)
[41] Towler M D, Allan N L, Harrison N M, Saunders V R, Mackrodt W C and Apra E 1994 *Phys. Rev.* B **50** 5041